Electronic Supplementary Material (ESI) for Energy & Environmental Science.

Supporting Information

Filling the Oxygen Vacancies in Co_3O_4 with Phosphorus: an Ultra-efficient Electrocatalyst for the Overall Water Splitting

Zhaohui Xiao, [†a] Yu Wang, [†b] Yu-Cheng Huang, [†c] Zengxi Wei, [a] Chung-Li Dong, [*d] Jianmin Ma, [a] Shaohua Shen, [e] Yafei Li, [*b] and Shuangyin Wang [*a]

[a] *State Key Laboratory of Chem/Bio-Sensing and Chemometrics, College of Chemistry and Chemical Engineering, Hunan University, Changsha, Hunan, 410082, P. R. China. E-mail: shuangyinwang@hnu.edu.cn*
[b] *College of Chemistry and Materials Science, Nanjing Normal University, Nanjing, Jiangsu, 210023, P.R. China. Email: liyafei@njnu.edu.cn.*
[c] *National Synchrotron Radiation Research Center, 101 Hsin-Ann Road, Hsinchu Science Park, Hsinchu 30076, Taiwan*
[d] *Department of Physics Tamkang University 151 Yingzhuan Rd., New Taipei City 25137, Taiwan. Email: cldong@mail.tku.edu.tw*
[e] *State Key Laboratory of Multiphase Flow in Power Engineering, Xi'an Jiaotong University, Xi'an, 710049, P.R. China*

† These authors contributed equally to this work.

Experimental

Preparation of Samples.

Pristine Co_3O_4 nanosheet arrays were prepared by the electrodeposition method in a three electrode cell with Ti mesh as working electrode and counter electrode, and saturated calomel electrode (SCE) as reference electrode at room temperature. The $Co(OH)_2$ was electrodeposited on Ti mesh (1 cm×1 cm) in a 0.05 M $Co(NO_3)_2$ aqueous electrolyte. The electrodeposition potential is -1.0 V (vs. SCE). After 10 minutes electrodeposition, the green Ti mesh was carefully rinsed several times with deionized water and ethanol. Then the sample was calcined at 300 °C for 2 hours with a heating rate of 1°C min^{-1} to transform into Co_3O_4 nanosheets. By the similar method, NiO-Ni foam ,Co_3O_4-Ni foam and Fe_3O_4-Ni foam electrodes were preparated by using commercial Ni foam (about 25.5 mg cm^{-2}) as substrates.

Synthesis of the FeNi alloy electrodes on Ni foams. Specifically, 3 mmol $Ni(NO_3)_2{\cdot}6H_2O$, 1 mmol $Fe(NO_3)_3{\cdot}6H_2O$, 20 mmol urea and 8 mmol NH_4F were completed dissolved in 80 ml deionized water under magnetic stirring. A nickel foam substrate was vertically immersed in the solution after chemically cleaned with acetone, methanol, and deionized water. The resulting solution with nickel foams were then sealed in a 100 ml Teflon-lined stainless steel autoclave, and maintained at 120 °C for 6 h, followed by struggle rinsing the nickel foams with deionized water and dried at 60 °C for 12 h.Then, the samples were annealed in H_2/Ar (H_2 10%) at 300 °C for 2h to obtain the FeNi alloy electrode.

To prepare P-Co_3O_4, NaH_2PO_2 was used as phosphorus source and placed at quartz tube front zone. Co_3O_4 nanosheet was placed at quartz tube posterior continuous cooling plasma zone. Ar was used as carrier gas (2 sccm) and convey phosphorus ion to pass the plasma zone. When the phosphorus source were heated to 250 °C, the Co_3O_4 nanosheets array was treated by plasma (13.56 MHz RF) with different irradiation time (0 min, 5 min, 10 min, 20 min, and 30 min) at 200W and 150 Pa. The treated Co_3O_4 for 20 min was used for detailed studies. The mass loading of P-Co_3O_4 on Ti mesh was determined to be about 0.4 mg cm^{-2}. V_O-Co_3O_4 was prepared by the same method but without NaH_2PO_2.

To prepare P@Co_3O_4, Co_3O_4 nanosheet arrays on Ti mesh and NaH_2PO_2 were placed at two separate positions in a quartz tube in the presence of NaH_2PO_2 at the upstream side of the quartz tube. The molar ratio of Co to P was 1:5. Subsequently, the samples were heated to 300 °C for 2 h at a heating rate of 2 °C min^{-1} under an Ar atmosphere in a tube furnace.

Electrochemical measurements.

The electrochemical measurements were carried out with a typical three-electrode system at the room temperature. A graphite rod was used as counter electrode and SCE as reference electrode and the obtained samples were used as the working electrode. The measurements were conducted in 1 M KOH or 0.1 M KOH at room temperature. The EIS test was performed at overpotential of 0.12 V for HER and 0.28 V for OER. Before the electrochemical test, the electrolyte was saturated by bubbling nitrogen or oxygen for 30 min. All data was presented with *IR* correction. The SCE reference electrode was calibrated before HER and OER measurements.[1] The calibration was conducted in a standard three-electrode system, where the SCE electrode served as the reference electrode, and two Pt wires served as working and counter electrodes. It yielded the equation: $E_{RHE} = E_{SCE} + 0.99$ V in 0.1 M KOH and $E_{RHE} = E_{SCE} + 1.05$ V in 1 M KOH. All the polarization curves run at a scanning rate of 5 $mV{\cdot}s^{-1}$. The mass loading of all kinds of electrocatalysts on Ti mesh were made sure to be about 0.4 mg cm^{-2}. The electrochemically active surface areas were estimated by measuring the capacitive current associated with double-layer charging from the scan-rate dependence of CVs.[2] The CVs measurements of working electrodes were carried out for two cycles between 1.14 and 1.24 V versus RHE with the scan rates of 2, 4, 6, 8, and 10 mV s^{-1}. The C_{dl} of various samples were estimated from plotting the ΔJ at different potential against the scan rate. The linear slope is equivalent to twice of the double-layer capacitance C_{dl}, which can be used to represent the electrochemically active surface area.[3]

Density functional theory (DFT) calculations.

In this work, DFT calculations were carried out using the plane-wave technique with exchange-correlation interactions modeled by GGA-PBE[4] functional, as implemented in the Vienna *ab* Initio Simulation package (VASP).[5] The ion–electron interactions were described by the projector-augmented plane wave approach.[6] All calculations were performed using a plane-wave cutoff energy of 460 eV with Fermi-level smearing of 0.1 eV for slabs and 0.01 eV for gas-phase species, and specially the GGA+U (U = 2 eV[7]) scheme introduced by Dudarev et al.[8] was employed to describe the strongly correlated d electrons of Co atom. For *k*-space sampling, the 4×4×4 and 3×4×1 Monkhorst-Pack grid were used in bulk and slabs calculations, respectively. The convergence threshold of energy and forces were set to be 1×10^{-5} eV and 0.04 eV/Å, respectively. Besides, the dipole corrections were employed in all slabs calculations.

Characterization.

The morphology and microstructure of the Co_3O_4 nanosheets were investigated by scanning electron microscope (SEM, Hitachi, S-4800) and transmission electron microscopy (TEM, Tecnai G2 F20). The crystal structures of the samples were characterized using powder X-ray diffraction (XRD, Bruker D8 Advance diffractometer, Cu Kα1). The Raman spectra were collected on a Raman spectrometer (Raman, Labram-010) using a 632 nm laser. The synchrotron EXAFS and XANES of Co K-edge were carried out at BL17C at National Synchrotron Radiation Research Center, Taiwan. The X-ray photoelectron spectroscopy (XPS) analysis was performed on an AXIS ULTRA X-ray photoelectron spectrometer (Al as the excitation source).

Supporting Results

DFT Calculations Detail.

For bulk Co_3O_4 with antiferromagnetic ground state, the lattice parameter is determined to ~8.12 Å, which is consistent well with the experiments (~8.09 Å[9]) and previous calculations (~8.12 Å[7, 10]). To explore the catalytic performance, the energetically favourable Co_3O_4 (110) plane is chosen as the active surface, since it is highly exposed in our as-synthesized Co_3O_4 and has been believed to play a crucial role in the detected high activity of Co_3O_4 catalysts[11]. Moreover, the Co_3O_4 (110) plane is modeled with Co_4O_4-termination as this type is more stable than another termination (Co_2O_4) in a wide range of chemical potential of oxygen[12]. All the periodic slabs are constructed with seven atomic layers with a vacuum space of 15 Å, of which only the top two layers are allowed to relax. Figure S21 shows the geometric structures of (110) plane slabs of pristine Co_3O_4, V_O-Co_3O_4, and P-Co_3O_4. Note that the energetically favourable oxygen vacancy and doped P is reported in the V_O-Co_3O_4 and P-Co_3O_4, respectively. The active surfaces have exposed two types of Co atoms, namely three-fold and four-fold coordinated Co, which are represented by Co_{3f} and Co_{4f}, respectively.

The adsorption free energy for adsorbates (ΔG_{ads}) in HER and OER, including H* (ΔG_{H*}), OOH* (ΔG_{OOH*}), O*(ΔG_{O*}), and OH* (ΔG_{OH*}), can be calculated by the following equation:

$$\Delta G_{ads} = \Delta E_{ads} + \Delta E_{ZPE} - T\Delta S$$

where ΔE_{ads} is the adsorption energy of adsorbates, and T (298.15 K in this work) is temperature. ΔE_{ZPE} and ΔS are the energy difference in zero point energy and entropy, respectively. For example, the hydrogen adsorption free energy (ΔG_{H*}) is expressed as $\Delta G_{H*} = \Delta E_{H*} + \Delta E_{ZPE} - \mathrm{T}\Delta S$. For adsorabtes, all 3N degrees of freedom are treated as harmonic vibrational motions with neglecting contributions from the slab. Note here that the entropy contributions from H* has been included to obtain more accurate ΔG_{H*}. The calculated zero-pint energy correction (E_{ZPE}), entropy contribution (TS), and the total free energy correction ($G - E_{elec}$) are listed in Table S5. Besides, the ΔE_{ads} for H*, OOH*, O*, and OH* can be calculated by the following equations:[13]

$$\Delta E_{H*} = E(\mathrm{H*}) - E(*) - 1/2E_{H2}$$

$$\Delta E_{OOH*} = E(\mathrm{OOH*}) - E(*) - (2E_{H2O} - 3/2E_{H2})$$

$$\Delta \mathrm{E}_{O*} = \mathrm{E(O*)} - E(*) - (E_{H2O} - E_{H2})$$

$$\Delta \mathrm{E}_{OH*} = \mathrm{E(OH*)} - E(*) - (E_{H2O} - 1/2E_{H2})$$

where E is the electronic energy form DFT. The solvent effects on OOH* and OH* have also been considered by using the Poissson-Boltzmann implicit solavtion model[14]; the dielectric constant ε is taken as 80 for water.

In alkaline medium, the OER process generally involves the following steps[15]:

$$* + OH^- \rightarrow OH* + e^- \quad S\ (1)$$

$$OH + OH^- \rightarrow O* + H_2O + e^- \quad S\ (2)$$

$$O* + OH^- \rightarrow OOH* + e^- \quad S\ (3)$$

$$OOH* + OH^- \rightarrow O_2 + H_2O + e^- + * \quad S\ (4)$$

where * denotes an adsorption site. On the basis of computational hydrogen electrode (CHE) model[16], the free energy change along the OER processes (ΔG_n, n = 1–4) at standard conditions can be derived as:

$$\Delta G_1 = \Delta G_{OH*}$$

$$\Delta G_2 = \Delta G_{O*} - \Delta G_{OH*}$$

$$\Delta G_3 = \Delta G_{OOH*} - \Delta G_{O*}$$

$$\Delta G_4 = 4.92 - \Delta G_{OOH*}$$

Then the theoretical overpotentials (η^t) for OER can be calculated using the equations:

$$G^{OER} = \max\{\Delta G_1, \Delta G_2, \Delta G_3, \Delta G_4\}$$

$$\eta^t = G^{OER}/e - 1.23\ \mathrm{V}$$

In accordance with the CHE model, the effects of electrode potential (U) and pH on OER can be treated as an energy shift to free energy change in the four electrochemical steps: $\Delta G_U = -eU$ and $\Delta G_{pH} = -k_B\mathrm{T}\ln 10 \times \mathrm{pH}$. The free energy diagram of OER shown in this paper has performed a potential correction to be standard.

Supporting figures and tables

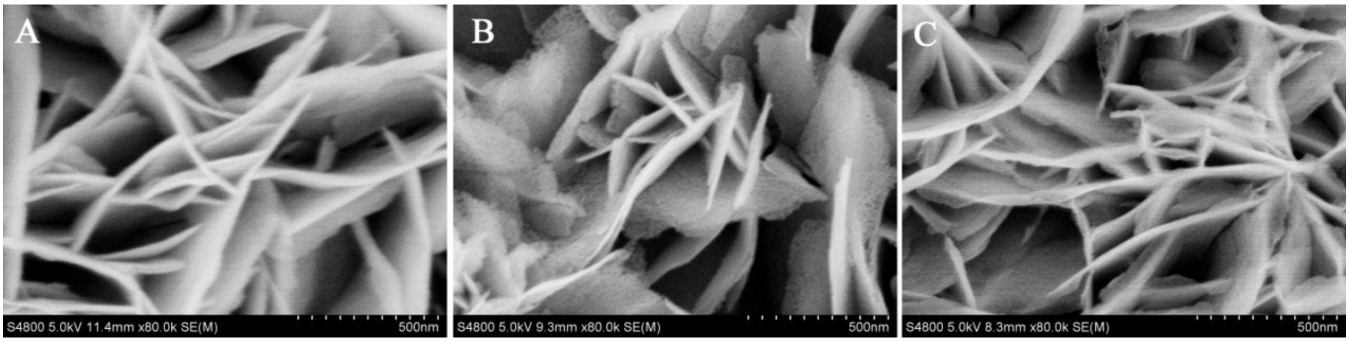

Figure S1. SEM images of (A) pristine Co_3O_4, (B) V_O-Co_3O_4 and (C) P-Co_3O_4 in Ti mesh.

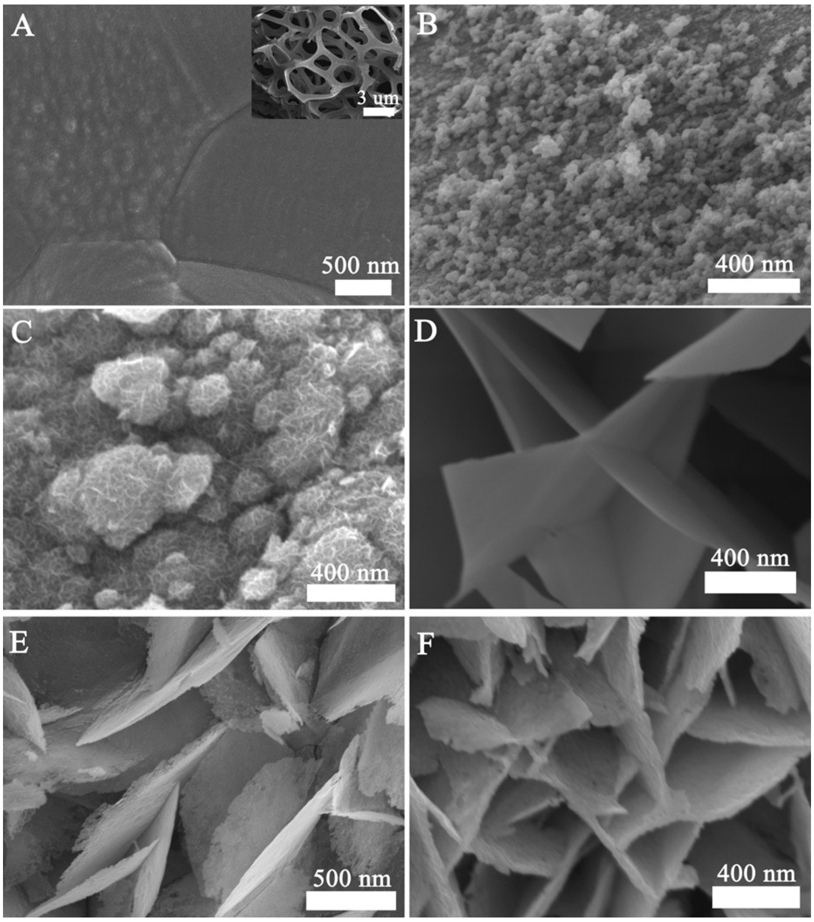

Figure S2. Raman spectra of (A) commercial Ni foam, (B) Fe_3O_4, (C) NiO, (D) FeNi alloy, (E) Co_3O_4 and (F) P-Co_3O_4. All these samples in Ni foam substrate.

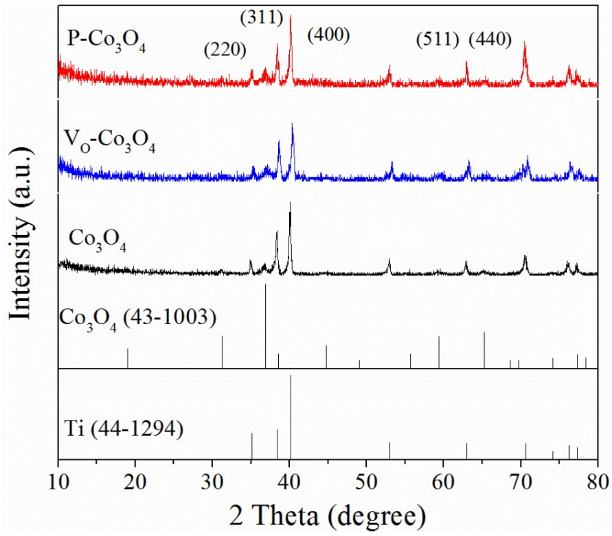

Figure S3. XRD of of pristine Co_3O_4, V_O-Co_3O_4 and P-Co_3O_4 on Ti mesh substrate.

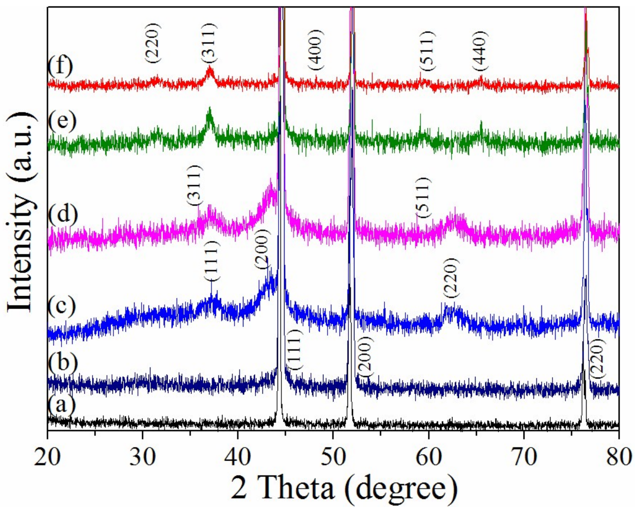

Figure S4. XRD of (a) commercial Ni foam, (b) FeNi alloy, (c) NiO, (d) Fe_3O_4, (e) Co_3O_4 and (f) P-Co_3O_4. All these samples in Ni foam substrate. The XRD patterns of these samples were corresponded to the standard JCPDS data: (a) 04-0850, (b) 38-0419, (c) 47-1049, (d) 26-1136, and (e, f) 43-1003, respectively.

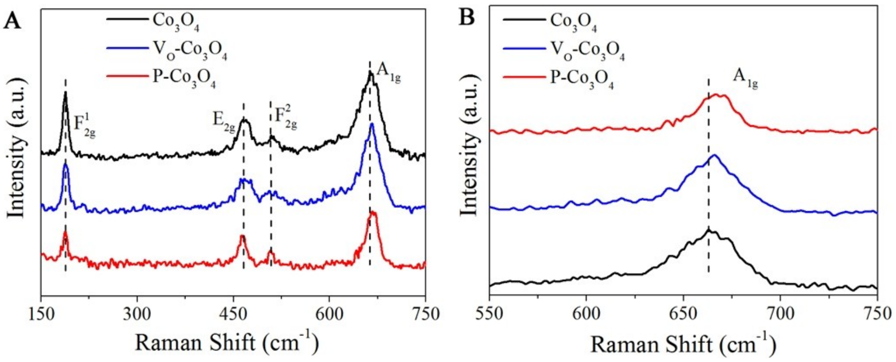

Figure S5. (A) Raman of pristine Co_3O_4, V_O-Co_3O_4 and P-Co_3O_4. (B) are local amplification images of (A). These samples in Ti mesh substrate.

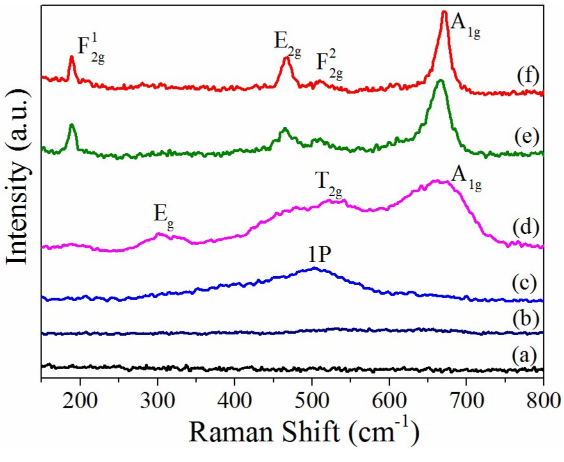

Figure S6. Raman of (a) commercial Ni foam, (b) FeNi alloy, (c) NiO, (d) Fe_3O_4, (e) Co_3O_4 and (f) P-Co_3O_4. All these samples on Ni foam substrate.

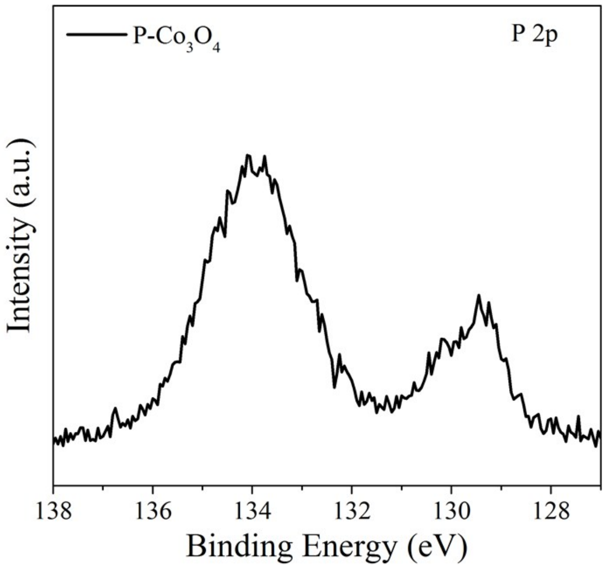

Figure S7. XPS spectrum of P 2p for P-Co_3O_4.

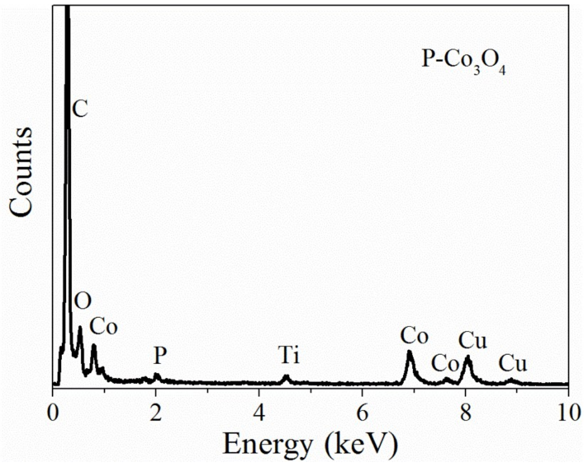

Figure S8. EDX spectra of P-Co_3O_4 nanosheets.

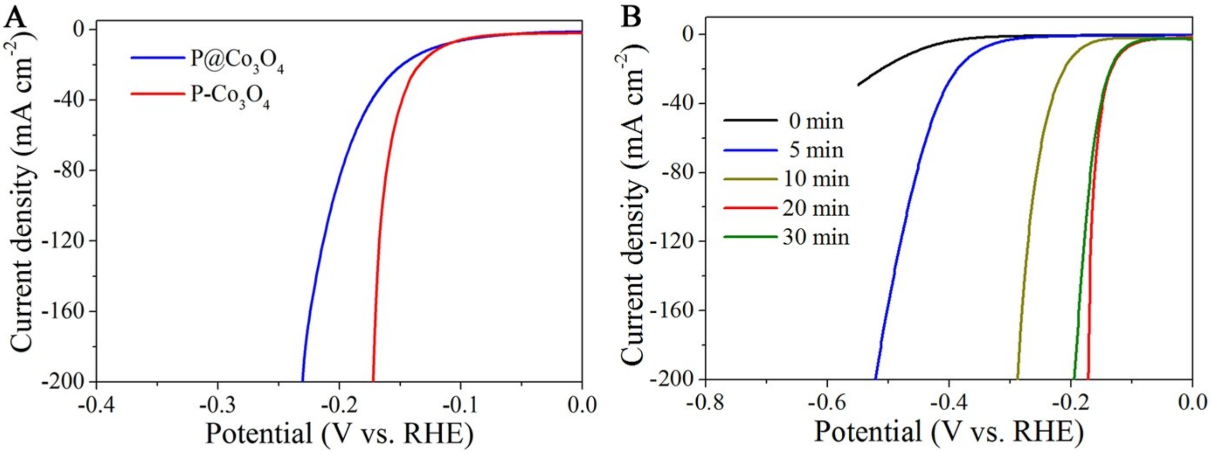

Figure S9. The polarization curves of different catalysts for OER in 1 M KOH (A) and (B).

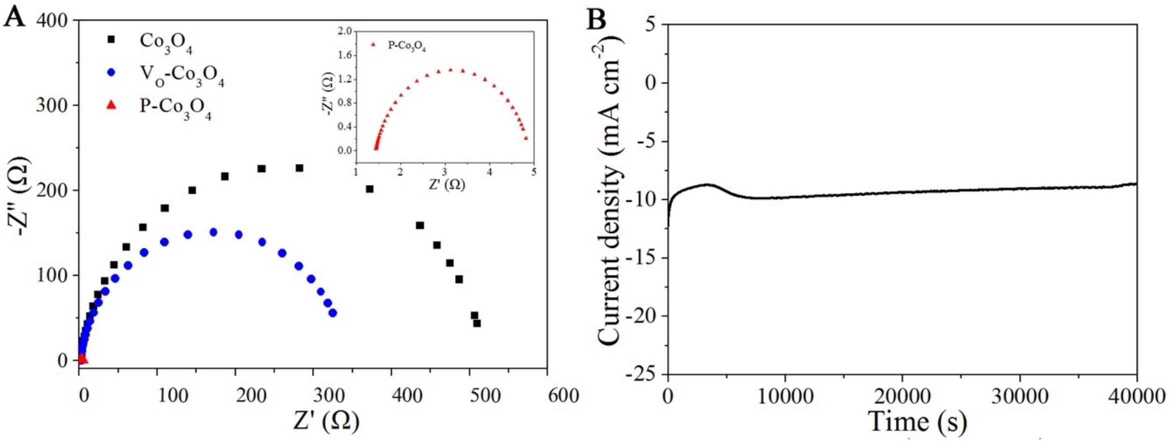

Figure S10. (A) Nyquist plots of HER on pristine Co_3O_4, V_O-Co_3O_4 and the P-Co_3O_4 in 1M KOH. (B) Time-dependent current curves for P-Co_3O_4 under a static potential at -0.12 V vs. RHE for 40000s.

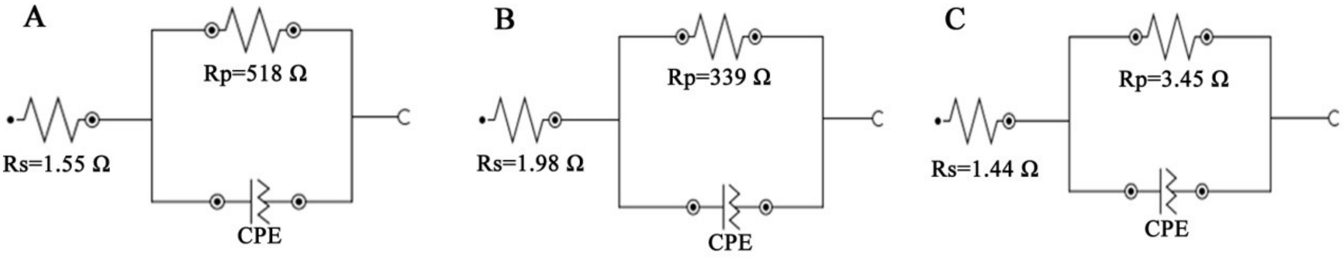

Figure S11. Electrochemical impedance spectroscopy (EIS) fitting results for pristine Co_3O_4, V_O-Co_3O_4 and P-Co_3O_4 based on the Nyquist plots (Figure S10A). Rs: Electrolyte resistance; Rp: Charge-transfer resistance; CPE: Constant-phase element.

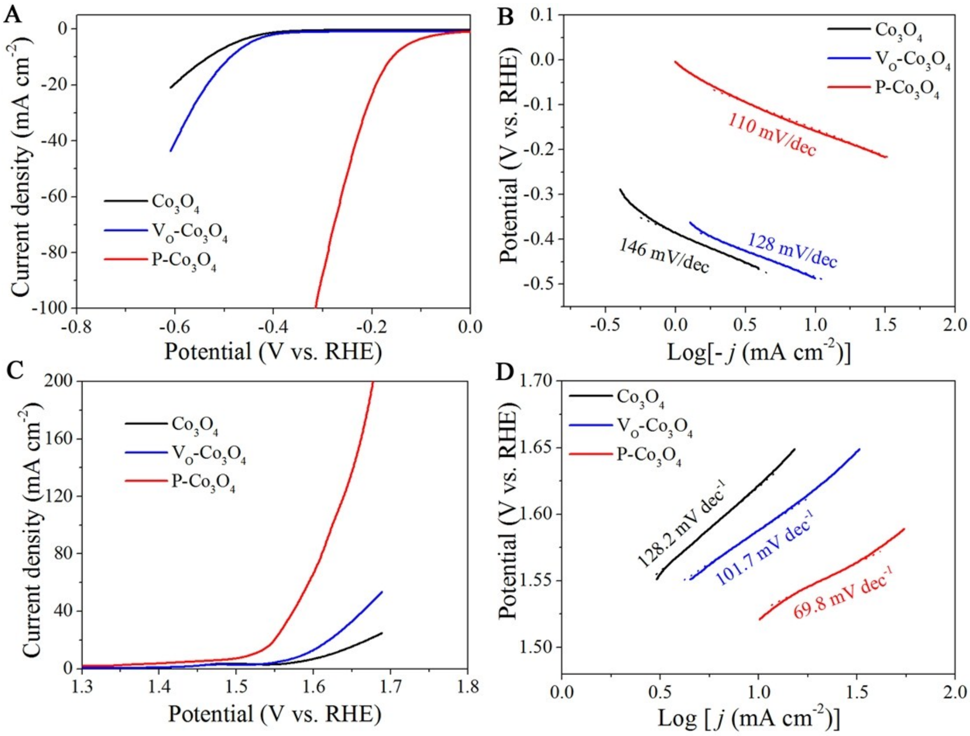

Figure S12. The polarization curves and Tafel plots of different catalysts for HER (A, C) and OER (B, D) in 0.1 M KOH.

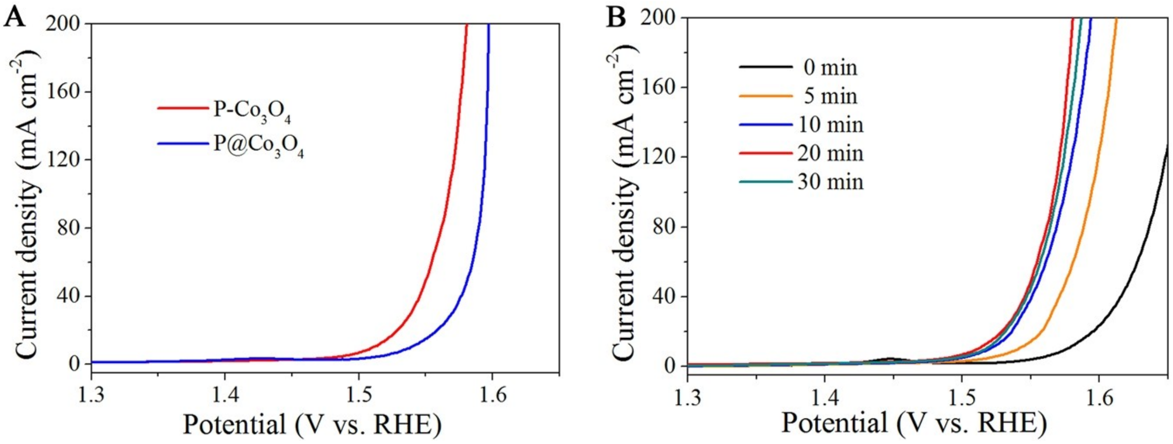

Figure S13. The polarization curves of different catalysts for OER in 1 M KOH (A) and (B).

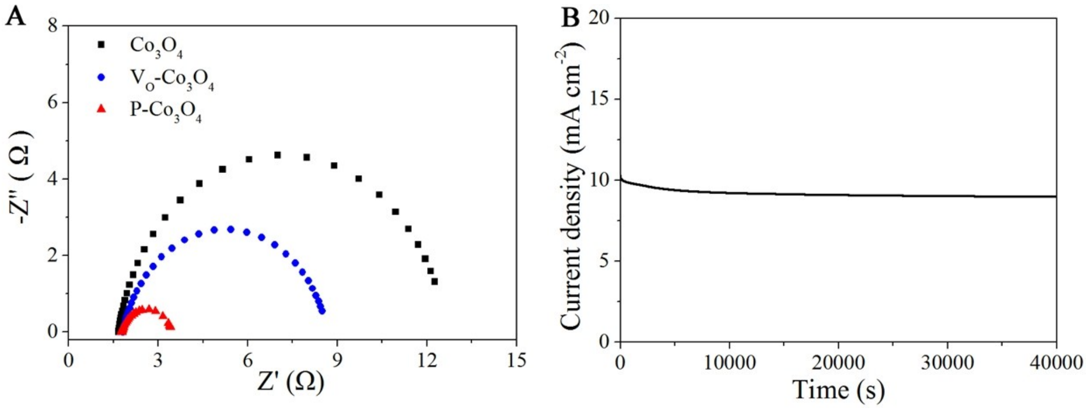

Figure S14. (A) Nyquist plots of OER on pristine Co_3O_4, V_O-Co_3O_4 and the P-Co_3O_4 in 1M KOH. (B) Polarization curves of initial LSV scans and after 40000s scans. The inset shows time-dependent current curves for P-Co_3O_4 under a static potential at 0.28 V vs. RHE for 40000s.

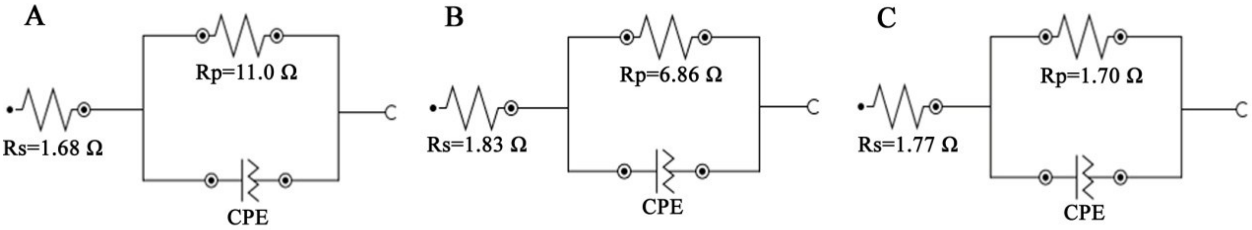

Figure S15. Electrochemical impedance spectroscopy (EIS) fitting results for pristine Co_3O_4, V_O-Co_3O_4 and P-Co_3O_4 based on the Nyquist plots (Figure S14A). Rs: Electrolyte resistance; Rp: Charge-transfer resistance; CPE: Constant-phase element.

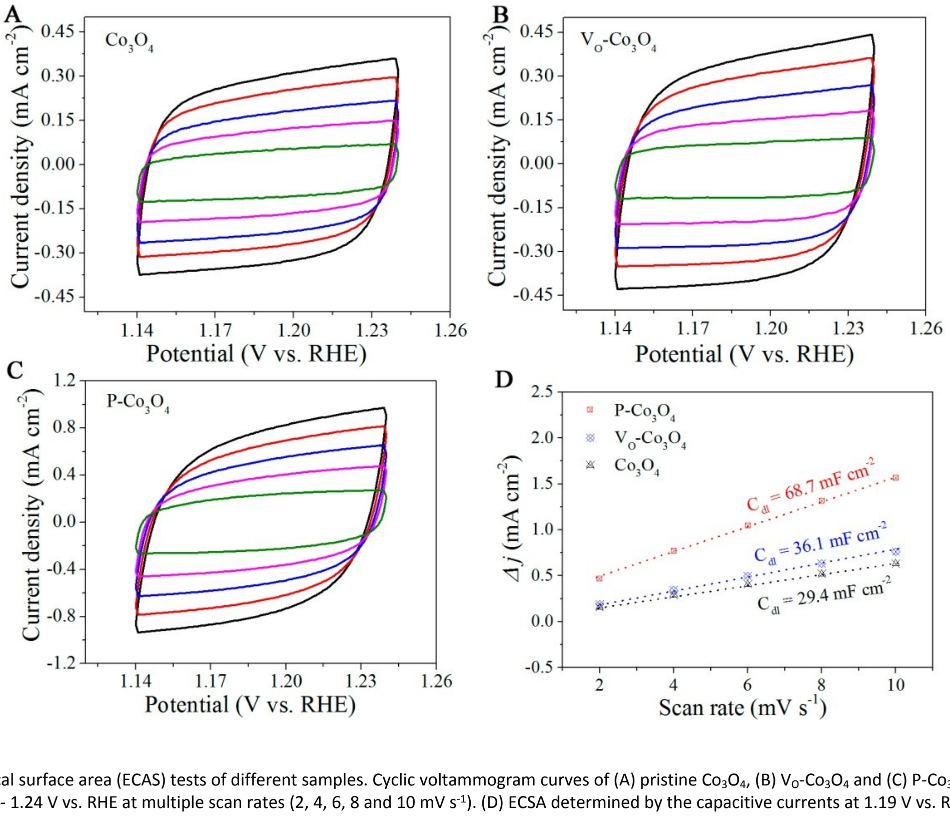

Figure S16. Electrochemical surface area (ECAS) tests of different samples. Cyclic voltammogram curves of (A) pristine Co_3O_4, (B) V_O-Co_3O_4 and (C) P-Co_3O_4 measured in the non-faradaic potential of 1.14 - 1.24 V vs. RHE at multiple scan rates (2, 4, 6, 8 and 10 mV s^{-1}). (D) ECSA determined by the capacitive currents at 1.19 V vs. RHE.

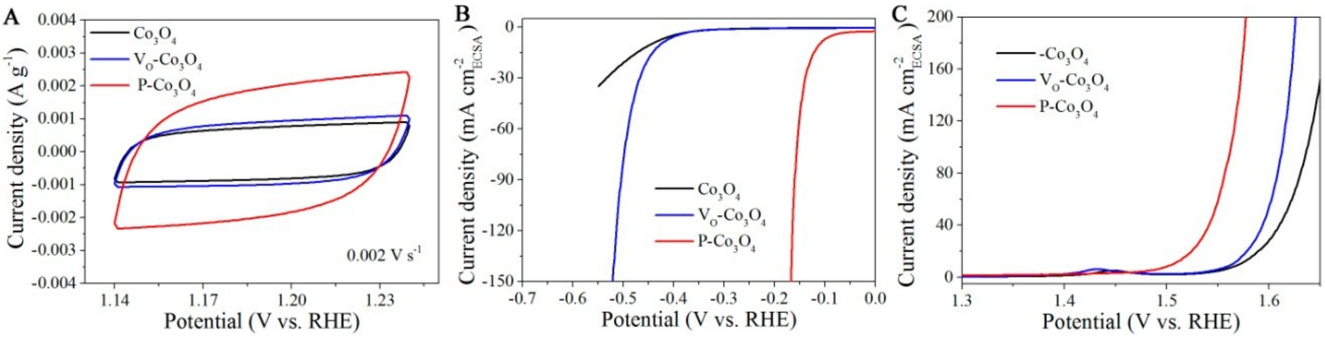

Figure S17. (A) Cyclic voltammograms of pristine Co_3O_4, V_O-Co_3O_4 and P-Co_3O_4 measured in the non-faradaic potential of 1.14 - 1.24 V vs. RHE at 0.002 V s^{-1}. The HER (B) and OER (C) performance of pristine Co_3O_4, V_O-Co_3O_4 and P-Co_3O_4 after the electrochemical active area (ECSA) normalization.

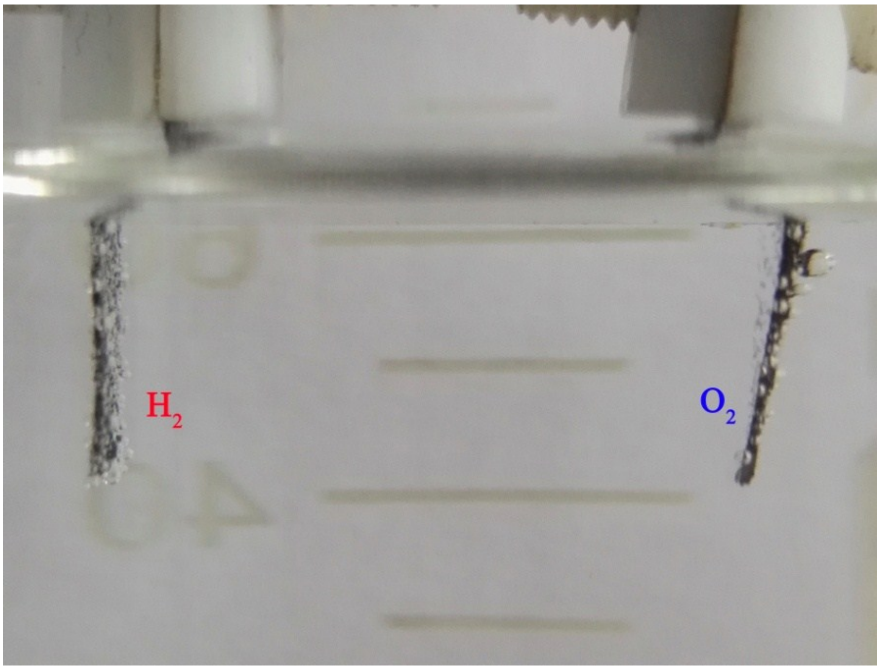

Figure S18. The photograph of an electrolysis cell using directly as the anode and cathode electrodes with generated bubbles on their surfaces.

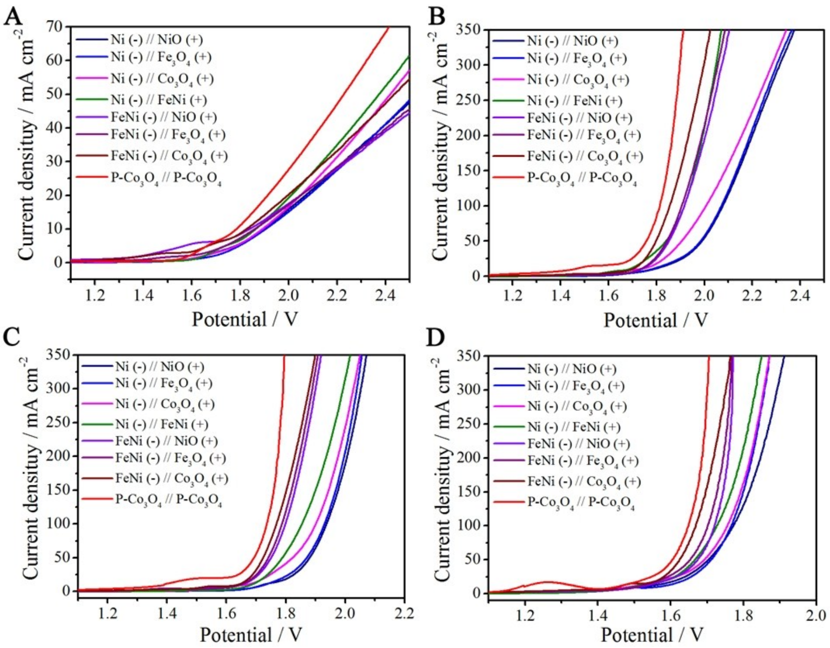

Figure S19. The polarization curves of different catalysts (Ni foam as substrates) for water splitting in different conditions: (A) 0.1 M KOH at 25 °C, (B) 1 M KOH at 25 °C, (C) 5 M KOH at 25 °C, and (D) 5 M KOH at 80 °C. Cathode: commercial Ni foam (Ni) or FeNi alloy (FeNi), and anode: metal-oxide or FeNi.

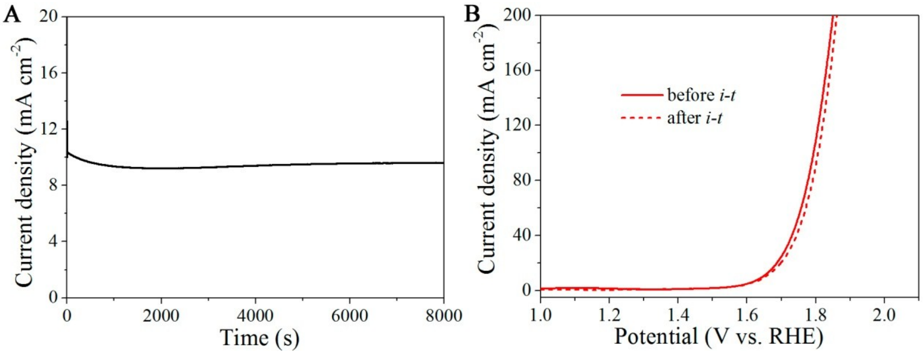

Figure S20. (A) Time-dependent current curves for P-Co_3O_4 under a static potential on 1.64V for 8000s in 1M KOH. (B) Polarization curves of initial scans and after 8000s.

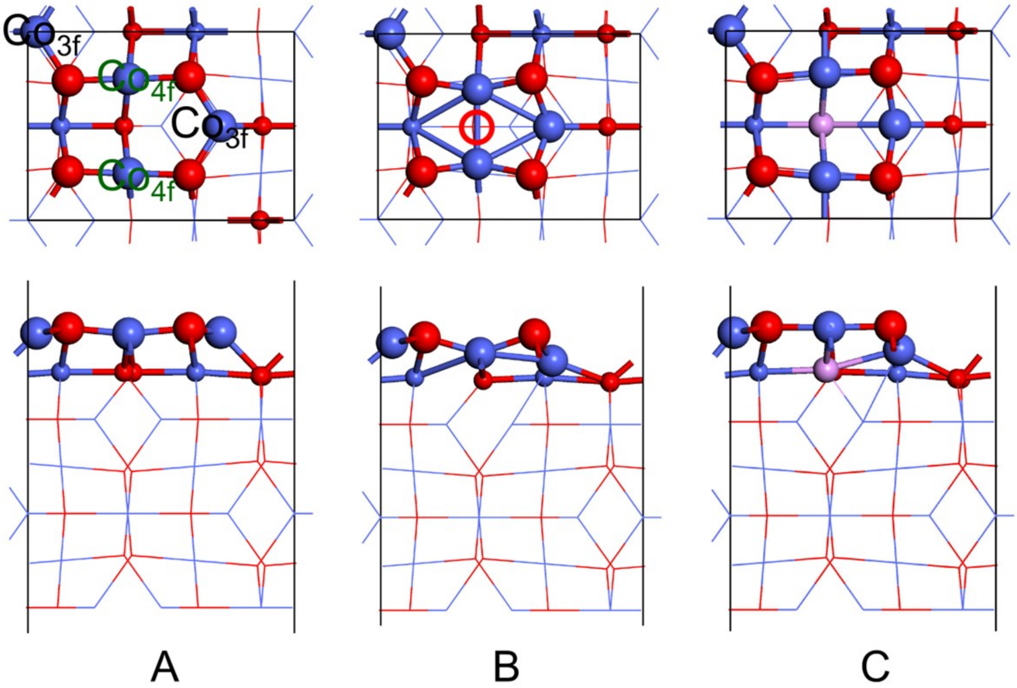

Figure S21. Top (upper) and side (bottom) views of pristine Co_3O_4 (A), V_O-Co_3O_4 (B) and P-Co_3O_4 (C). The sky blue, red, and pink balls represent Co, O, and P atoms, respectively.

The turnover frequency (TOF) is a very important kinetic parameter for HER and OER.[2a, 17] TOF is the intrinsic properties of the catalysts, which is important for evaluating the performance of the catalysts. Its calculation of the catalysts: The TOF value is calculated from the equation.

$$TOF= (j×A)/(4×F×m)$$

j is the current density at overpotential of 0.28 V for OER and 0.12V for HER. A is the geometry area of the Ti mesh electrode. F is the faraday constant (a value of 96485 C mol^{-1}). m is the number of moles of the active materials that are deposited onto the Ti mesh. All the Co atoms were assumed to be accessible for catalysis the HER or OER. As summarized in the Table S1, The estimated TOF of P-Co_3O_4 at the overpotential of 0.028V is higher than the pristine Co_3O_4 and V_O-Co_3O_4. These electrochemical results indicated that electrocatalytic activities of P-Co_3O_4 was significantly improved by the P filled the surface oxygen vacancies of Co_3O_4 in the plasma-engraved process.

Table S1. The turnover frequency (TOF) of Co_3O_4 nanosheets were estimated for HER and OER in 1 M KOH solution.

Sample	HER (1 M KOH)	OER (1 M KOH)
pristine Co_3O_4	$7.05*10^{-4}$	$2.73*10^{-3}$
V_O-Co_3O_4	$9.23*10^{-4}$	$3.29*10^{-3}$
P-Co_3O_4	$1.83*10^{-2}$	$1.58*10^{-2}$

Table S2. Comparison of the HER activity of the P-Co_3O_4 with other Co-based electrocatalysts in 1M KOH.

Catalyst	Onset Potential (V)	10.0 (mA cm^{-2})	Tafel slope (mV dec^{-1})	Mass loading (mg cm^{-2})
P-Co_3O_4 (This work)	0.05	0.12	51.6	0.4
Co_3O_4 NCs[18]	0.05	0.155	115	0.35
CoP/CC[19]	0.08	0.209	129	0.92
Co-P/NC[20]	~0.07	0.154	51	1
Co_3O_4-MTA[21]	0.10	~0.17	98	NA
CoP/G[22]	~0.10	0.154	NA	0.4
CoP[22]	~0.13	0.201	NA	0.4
Co/CoP[23]	~0.05	0.138	64	NA
CoP@BCN-1[24]	~0.05	0.215	52	0.4

Table S3. Comparison of the OER activity of the P-Co_3O_4 with other Co-based electrocatalysts in 1M KOH.

Catalyst	Onset Potential (V)	10.0 (mA cm^{-2})	Tafel slope (mV dec^{-1})	Mass loading (mg cm^{-2})
P-Co_3O_4 (This work)	1.46	1.51	52	0.4
Co_3O_4@C-MWCNTs[25]	1.50	1.55	62	0.29
Co_3O_4/N -rmGO[26]	1.50	1.54	67	1
Co_3O_4 NCs[18]	1.52	1.61	101	0.35
CoO_x@CN[27]	NA	1.49	NA	1
Co_3O_4/$NiCo_2O_4$ DSNCs[28]	1.53	1.57	88	1
Sandwich-like CoP/C[29]	~1.48	1.56	53	0.36
Co-P film[30]	1.53	1.56	47	1.0
Co-P/NC[20]	~1.50	~1.55	51	1

CoP NR/C[31]	~1.49	1.55	71	0.71
CoP/G[22]	NA	1.522	80	0.4
NiFe/NiFe:Pi[32]	1.43	1.527	38	NA
$NiCo_2O_4$[33]	~1.48	~1.52	30	0.285
CC@$NiCo_2O_4$[34]	1.49	1.57	72	0.6
CC@Co_3O_4[34]	1.52	1.61	75	0.6
NiCoP NPs/Ti[35]	~1.49	1.54	52	0.75

Table S4. Comparison of the water splitting activity of the P-Co_3O_4 with other electrocatalysts in different conditions of alkaline solutions.

Catalyst	0.1 M KOH 25 °C	1 M KOH 25 °C	5 M KOH 25 °C	5 MKOH 80 °C
Ni (-) // NiO (+)	30.12 mA cm^{-2} - 2.23 V	50 mA cm^{-2} – 1.99 V	50 mA cm^{-2} – 1.88 V	50 mA cm^{-2} – 1.70 V
Ni (-) // Fe_3O_4 (+)	29.39 mA cm^{-2} - 2.23 V	50 mA cm^{-2} – 1.98 V	50 mA cm^{-2} – 1.88 V	50 mA cm^{-2} – 1.71 V
Ni (-) // Co_3O_4 (+)	33.78 mA cm^{-2} - 2.23 V	50 mA cm^{-2} – 1.91 V	50 mA cm^{-2} – 1.82 V	50 mA cm^{-2} – 1.69 V
Ni (-) // FeNi (+)	37.43 mA cm^{-2} - 2.23 V	50 mA cm^{-2} – 1.84 V	50 mA cm^{-2} – 1.78 V	50 mA cm^{-2} – 1.66 V
FeNi (-) // NiO (+)	29.45 mA cm^{-2} - 2.23 V	50 mA cm^{-2} – 1.85 V	50 mA cm^{-2} – 1.75 V	50 mA cm^{-2} – 1.67 V
FeNi (-) // Fe_3O_4 (+)	30.11 mA cm^{-2} - 2.23 V	50 mA cm^{-2} – 1.84 V	50 mA cm^{-2} – 1.74 V	50 mA cm^{-2} – 1.65 V
FeNi (-) // Co_3O_4 (+)	35.24 mA cm^{-2} - 2.23 V	50 mA cm^{-2} – 1.80 V	50 mA cm^{-2} – 1.72 V	50 mA cm^{-2} – 1.63 V
P-Co_3O_4 // P-Co_3O_4	50 mA cm^{-2} - 2.23 V	50 mA cm^{-2} – 1.76 V	50 mA cm^{-2} – 1. 69 V	50 mA cm^{-2} – 1.61 V 100 mA cm^{-2} – 1.65 V

Table S5. Calculated zero-pint energy correction (E_{ZPE}), entropy contribution (TS), and the total free energy correction ($G - E_{elec}$) of the studied systems.

Species	E_{ZPE} (eV)	$-TS$ (eV)	$G - E_{elec}$ (eV)
H_2	0.270	−0.410	−0.140
H_2O	0.560	−0.670	0.110
H* on Co_3O_4	0.205	−0.004	0.201
OOH* on Co_3O_4	0.451	−0.158	0.293
O* on Co_3O_4	0.073	−0.040	0.033
OH* on Co_3O_4	0.380	−0.057	0.323
H* on V_O-Co_3O_4	0.221	−0.003	0.218
OOH* on V_O-Co_3O_4	0.443	−0.192	0.251
O* on V_O-Co_3O_4	0.065	−0.074	−0.009
OH* on V_O-Co_3O_4	0.358	−0.084	0.274
H* on P-Co_3O_4	0.188	−0.005	0.183
OOH* on P-Co_3O_4	0.422	−0.183	0.239
O* on P-Co_3O_4	0.066	−0.073	−0.007
OH* on P-Co_3O_4	0.359	−0.072	0.287

References

[1] aS. Dou, L. Tao, J. Huo, S. Wang, L. Dai, *Energy & Environmental Science* **2016**, *9*, 1320-1326; bZ. Xiao, X. Huang, L. Xu, D. Yan, J. Huo, S. Wang, *Chemical Communications* **2016**, *52*, 13008-13011.

[2] aC. C. L. McCrory, S. Jung, J. C. Peters, T. F. Jaramillo, *Journal of the American Chemical Society* **2013**, *135*, 16977-16987; bT. Zhai, L. Wan, S. Sun, Q. Chen, J. Sun, Q. Xia, H. Xia, *Advanced materials* **2017**, *29*.

[3] J. Li, Y. Wang, T. Zhou, H. Zhang, X. Sun, J. Tang, L. Zhang, A. M. Al-Enizi, Z. Yang, G. Zheng, *Journal of the American Chemical Society* **2015**, *137*, 14305-14312.

[4] J. P. Perdew, K. Burke, M. Ernzerhof, *Physical Review Letters* **1996**, *77*, 3865-3868.

[5] aG. Kresse, J. Hafner, *Physical Review B* **1993**, *47*, 558-561; bG. Kresse, J. Furthmüller, *Computational Materials Science* **1996**, *6*, 15-50.

[6] aP. E. Blöchl, *Physical Review B* **1994**, *50*, 17953-17979; bG. Kresse, D. Joubert, *Physical Review B* **1999**, *59*, 1758-1775.

[7] D.-e. Jiang, S. Dai, *Physical Chemistry Chemical Physics* **2011**, *13*, 978-984.

[8] S. L. Dudarev, G. A. Botton, S. Y. Savrasov, C. J. Humphreys, A. P. Sutton, *Physical Review B* **1998**, *57*, 1505-1509.

[9] P. Dutta, M. S. Seehra, S. Thota, J. Kumar, *Journal of Physics: Condensed Matter* **2008**, *20*, 015218.

[10] P. Broqvist, I. Panas, H. Persson, *Journal of Catalysis* **2002**, *210*, 198-206.

[11] aX. Xie, Y. Li, Z.-Q. Liu, M. Haruta, W. Shen, *Nature* **2009**, *458*, 746-749; bC. Y. Ma, Z. Mu, J. J. Li, Y. G. Jin, J. Cheng, G. Q. Lu, Z. P. Hao, S. Z. Qiao, *Journal of the American Chemical Society* **2010**, *132*, 2608-2613.

[12] J. Chen, A. Selloni, *Physical Review B* **2012**, *85*, 085306.

[13] I. C. Man, H.-Y. Su, F. Calle-Vallejo, H. A. Hansen, J. I. Martínez, N. G. Inoglu, J. Kitchin, T. F. Jaramillo, J. K. Nørskov, J. Rossmeisl, *ChemCatChem* **2011**, *3*, 1159-1165.

[14] K. Mathew, R. Sundararaman, K. Letchworth-Weaver, T. Arias, R. G. Hennig, *The Journal of chemical physics* **2014**, *140*, 084106.

[15] X. Cui, P. Ren, D. Deng, J. Deng, X. Bao, *Energy & Environmental Science* **2016**, *9*, 123-129.

[16] J. K. Nørskov, J. Rossmeisl, A. Logadottir, L. Lindqvist, J. R. Kitchin, T. Bligaard, H. Jónsson, *The Journal of Physical Chemistry B* **2004**, *108*, 17886-17892.

[17] A. J. Esswein, M. J. McMurdo, P. N. Ross, A. T. Bell, T. D. Tilley, *The Journal of Physical Chemistry C* **2009**, *113*, 15068-15072.

[18] S. Du, Z. Ren, J. Zhang, J. Wu, W. Xi, J. Zhu, H. Fu, *Chemical Communications* **2015**, *51*, 8066-8069.

[19] J. Tian, Q. Liu, A. M. Asiri, X. Sun, *Journal of the American Chemical Society* **2014**, *136*, 7587-7590.

[20] B. You, N. Jiang, M. Sheng, S. Gul, J. Yano, Y. Sun, *Chemistry of Materials* **2015**, *27*, 7636-7642.

[21] Y. P. Zhu, T. Y. Ma, M. Jaroniec, S. Z. Qiao, *Angewandte Chemie International Edition* **2017**, *56*, 1324-1328.

[22] H. Huang, C. Yu, J. Yang, C. Zhao, X. Han, Z. Liu, J. Qiu, *ChemElectroChem* **2016**, *3*, 719-725.

[23] H. Wang, S. Min, Q. Wang, D. Li, G. Casillas, C. Ma, Y. Li, Z. Liu, L.-J. Li, J. Yuan, M. Antonietti, T. Wu, *ACS Nano* **2017**, *11*, 4358-4364.

[24] H. Tabassum, W. Guo, W. Meng, A. Mahmood, R. Zhao, Q. Wang, R. Zou, *Advanced Energy Materials* **2017**, 1601671-n/a.

[25] X. Li, Y. Fang, X. Lin, M. Tian, X. An, Y. Fu, R. Li, J. Jin, J. Ma, *Journal of Materials Chemistry A* **2015**, *3*, 17392-17402.

[26] Y. Liang, Y. Li, H. Wang, J. Zhou, J. Wang, T. Regier, H. Dai, *Nat Mater* **2011**, *10*, 780-786.

[27] H. Jin, J. Wang, D. Su, Z. Wei, Z. Pang, Y. Wang, *Journal of the American Chemical Society* **2015**, *137*, 2688-2694.

[28] H. Hu, B. Guan, B. Xia, X. W. Lou, *Journal of the American Chemical Society* **2015**, *137*, 5590-5595.

[29] Y. Bai, H. Zhang, Y. Feng, L. Fang, Y. Wang, *Journal of Materials Chemistry A* **2016**, *4*, 9072-9079.

[30] N. Jiang, B. You, M. Sheng, Y. Sun, *Angewandte Chemie International Edition* **2015**, *54*, 6251-6254.

[31] J. Chang, Y. Xiao, M. Xiao, J. Ge, C. Liu, W. Xing, *ACS Catalysis* **2015**, *5*, 6874-6878.

[32] Y. Li, C. Zhao, *ACS Catalysis* **2017**, *7*, 2535-2541.

[33] J. Bao, X. Zhang, B. Fan, J. Zhang, M. Zhou, W. Yang, X. Hu, H. Wang, B. Pan, Y. Xie, *Angewandte Chemie* **2015**, *127*, 7507-7512.

[34] C. Guan, X. Liu, W. Ren, X. Li, C. Cheng, J. Wang, *Advanced Energy Materials* **2017**, 1602391-n/a.

[35] C. Wang, J. Jiang, T. Ding, G. Chen, W. Xu, Q. Yang, *Advanced Materials Interfaces* **2016**, *3*, 1500454-n/a.